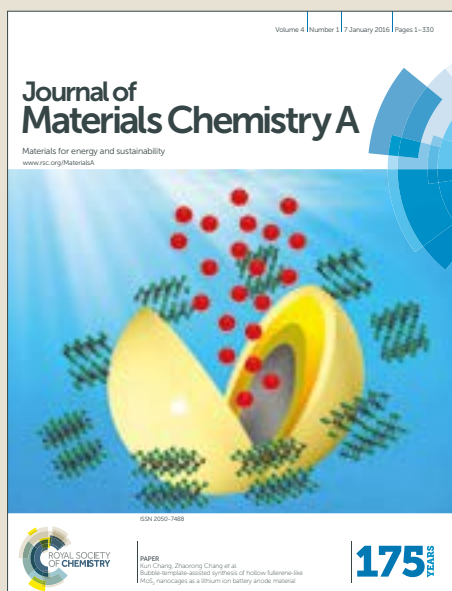


Journal of Materials Chemistry A

Accepted Manuscript



This article can be cited before page numbers have been issued, to do this please use: Q. Mu, W. Zhu, G. Yan, Y. Lian, Y. Yao, Q. Li, Y. Tian, P. Zhang, Z. Deng and Y. Peng, *J. Mater. Chem. A*, 2018, DOI: 10.1039/C8TA06151C.



This is an Accepted Manuscript, which has been through the Royal Society of Chemistry peer review process and has been accepted for publication.

Accepted Manuscripts are published online shortly after acceptance, before technical editing, formatting and proof reading. Using this free service, authors can make their results available to the community, in citable form, before we publish the edited article. We will replace this Accepted Manuscript with the edited and formatted Advance Article as soon as it is available.

You can find more information about Accepted Manuscripts in the [author guidelines](#).

Please note that technical editing may introduce minor changes to the text and/or graphics, which may alter content. The journal's standard [Terms & Conditions](#) and the ethical guidelines, outlined in our [author and reviewer resource centre](#), still apply. In no event shall the Royal Society of Chemistry be held responsible for any errors or omissions in this Accepted Manuscript or any consequences arising from the use of any information it contains.

Activity and Selectivity Regulation through the Size of Cobalt Active Sites in Photocatalytic CO₂ Reduction

Qiaoqiao Mu ^{a,b}, Wei Zhu ^{a,b}, Gangbin Yan ^{a,b}, Yuebin Lian ^{a,b}, Yuanzhou Yao ^{a,b}, Qin Li ^{a,b}, Yuyu Tian ^c, Peng Zhang ^c, Yang Peng ^{a, b, *}, Zhao Deng ^{a, b, *}

ZIF Received 00th January 20xx,
Accepted 00th January 20xx

DOI: 10.1039/x0xx00000x

www.rsc.org/

The development of efficient and economical catalysts for photocatalytic reduction of CO₂ into chemical feedstocks is highly desirable for addressing both the global energy crisis and carbon emission problem. Herein, a series of carbonized cobalt composites derived from the bimetallic Zn/Co zeolite imidazolate frameworks (C-BMZIFs) are synthesized and used as the co-catalysts for [Ru(bpy)₃]²⁺ mediated photocatalytic CO₂ reduction under visible light irradiation. Varying the Zn/Co ratio allows regulating the size of Co active sites, which further differentiates their catalytic activity towards CO₂ reduction and H₂ evolution, resulting in tunable CO/H₂ ratio in the produced syngas. Among all investigated configurations, the C-BMZIF with a Zn/Co ratio of 3:1 demonstrates the highest CO yield of 1.1 × 10⁴ μmol/g/h, owing to the optimal balance between the quantity of active sites and the activity of each individual site. Consequently, this work provides insight into the design of stable MOFs-derived co-catalysts for efficient photo-reduction of CO₂, and offers an alternative solution for photocatalytic syngas production with tunable CO/H₂ ratio.

1. Introduction

Artificial photosynthesis aiming for the photocatalytic conversion of CO₂ into renewable fuels and chemical feedstocks has been regarded as a promising solution to simultaneously reduce environmental pollutions and alleviate the growing energy crisis.¹⁻⁴ A key aspect in realizing this goal is the development of highly efficient photocatalysts that enable to greatly lower the kinetic energy barrier in CO₂ reduction, which requires to break the stable C=O bond (750 kJ mol⁻¹) and is initiated by the formation of the thermodynamically unfavorable intermediate CO₂^{•-} upon accepting the first electron ($E^0(\text{CO}_2^{\bullet-}/\text{CO}_2) = -1.49 \text{ V vs. RHE}$).⁴⁻⁶ In such context, tremendous efforts have been devoted to develop potent and economic catalysts for the CO₂ reduction reaction (CO₂ RR).^{2, 7-15} Of the diverse reduction products, CO has been mostly obtained, as the conversion from CO₂ to CO only involves two electron transfer and a redox potential of -0.12 V vs. RHE.^{8, 16} However, in many catalytic systems involving H₂O as the proton source, this potential also conveniently triggers the hydrogen evolution reaction (HER), which has been viewed as a major competing reaction for CO₂ RR.¹⁷⁻¹⁹ While in many applications a high selectivity towards CO is

certainly desired because of the simplification of the following separation process, in some applications, especially for the use of syngas containing CO and H₂ as the chemical feedstock for Fischer-Tropsch reactions, the HER can be indeed beneficial and utilized for simultaneous H₂ production.^{17, 20, 21} This is even more so if one can conveniently regulate the selectivity, and thus the CO/H₂ ratio in the obtained syngas, targeting for the synthesis of specific chemicals.^{17, 18, 20}

Metal-organic frameworks (MOFs), capable of integrating CO₂ capture and its catalytic conversion together, represents a class of porous materials that have been demonstrated as efficient co-catalysts, in work with photosensitizers together, for photocatalytic CO₂ reduction.^{3, 10-12, 22-24} They act as the catalytic booster by promoting the kinetics of both charge separation from the photosensitizer and surface reaction for CO₂ conversion.^{12, 25} Taking the Zeolitic Imidazolate Frameworks (ZIFs) family as an example, previous studies have shown Co-ZIF-9 and Co-ZIF-67 with various nanostructured morphology are capable of promoting the CO₂ photoreduction by integrating the electron-mediating function of cobalt species spatially confined by imidazolate motifs in the heterogeneous crystalline scaffolds.^{3, 12} Particularly, a leaf-like morphology of the two-dimensional laminated Co-ZIF-67 further enhances its capability of CO₂ reduction by facilitating the electron transfer between the co-catalyst and the photosensitizer [Ru(bpy)₃]²⁺.¹⁰ Nevertheless, despite of these intriguing observations, a significant challenge remains to balance the photocatalytic properties with MOF stability, especially when water is used as both solvent and proton donor.^{16, 26-29} To overcome this problem, carbonization of MOFs at high temperature to construct heteroatom-doped metal-carbon complexes with rich active sites for CO₂ RR has been pursued as an alternate solution.

^a Soochow Institute for Energy and Materials Innovations, College of Energy, Soochow University, Suzhou 215006, P. R. China.

^b Key Laboratory of Advanced Carbon Materials and Wearable Energy Technologies of Jiangsu Province, Soochow University, Suzhou 215006, P. R. China.

*Email: zdeng@suda.edu.cn; ypeng@suda.edu.cn.

^c State Key Lab of Metal Matrix Composites, School of Materials Science and Engineering, Shanghai Jiao Tong University, Shanghai, 200240, P. R. China
Electronic Supplementary Information (ESI) available: [details of any supplementary information available should be included here]. See DOI: 10.1039/x0xx00000x

Using carbonized MOFs as nanostructured scaffold for hosting metal complexes and nanoparticles as electrocatalytically active sites for CO₂ RR, the faradic efficiency towards CO production and the thus resulted component ratio in the electrochemically produced syngas can be effectively tuned through the modulation of local coordination environment.^{6, 30-33} For instance, by ball-milling the iron precursors with Zn-ZIF-8 together, Jaouen et al. prepared a set of Fe-N-C electrocatalysts containing both single-Fe-atom centers and Fe-containing nanoparticles (NPs), and found while the former is responsible for CO₂ reduction into CO, the latter mainly catalyze hydrogen evolution.⁸ Similarly, through ionic exchange of Zn-ZIF-8, Li et al. compared Ni single atoms with nanoparticles distributed in nitrogen-doped porous carbon for electroreduction of CO₂ and also revealed atomically dispersed Ni active sites exhibit higher selectivity towards CO production.³⁴ In a later study, utilizing the coordination chemistry in the bimetallic Zn-Co ZIF-8 the same group fabricated atomically dispersed Co catalysts and successfully tuned the coordination number of single Co atoms by varying the pyrolysis temperature.³² They found the less coordinated Co-N₂ chemistry demonstrated significantly higher CO faradic efficiency than both Co-N₄ and Co NPs, with the latter two produced H₂ in majority. Almost at the same time, Bao et al. synthesized coordinatively unsaturated nickel-nitrogen (Ni-N) sites doped within porous carbon, derived from the pyrolysis of Zn/Ni bimetallic ZIF-8 with varied Zn/Ni ratios, and revealed similar trend in the composition of produced syngas as tuned by the Ni-N_x coordination chemistry.³⁵ All these electrocatalytic studies unanimously demonstrate a structure-selectivity relationship across all investigated catalytic systems, with the CO/H₂ ratio in the product governed by the particle size and coordination chemistry of the metal active sites. However, to our best knowledge, similar structure-selectivity illustration hasn't been seen in photocatalytic CO₂ reduction, and further mechanistic insights into the observed selectivity are desired.

Based on the above considerations, herein a series of carbonized bimetallic Zn/Co composites template by ZIFs with the uniform rhombic dodecahedral structure and various Zn/Co ratios have been successfully prepared by high-temperature pyrolysis for photocatalytic applications. We find the presence of Zn in the bimetallic frameworks enables to not only tune the overall MOF particle size, but also effectively control the size of Co active sites on the carbonized MOF scaffolds. When used as the co-catalyst for photocatalytic reduction of CO₂ under visible light irradiation with [Ru(bpy)₃]²⁺ (bpy = 2,2'-bipyridine) as the photosensitizer and triethanolamine (TEOA) as the electron donor, the carbonized ZIF composite with a Zn/Co ratio of 3:1 delivered a high CO yield of 1.1 × 10⁴ μmol·g⁻¹·h⁻¹. More importantly, by regulating the size of Co active sites, the co-catalysts with different Zn/Co ratio enable to effectively tune the product selectivity in the produced syngas. Consequently, this study, by illustrating the structure-activity-selectivity relationship of the metal active sites on the carbonized bimetallic ZIFs, sheds new light on the design of non-noble metal photocatalysts for high-efficiency CO₂ RR, as well as tunable syngas synthesis.³⁶

2. Experimental section

2.1. Chemicals

Cobalt nitrate hexahydrate (Co(NO₃)₂·6H₂O) was purchased from Sinopharm Chemical Reagent Co., Ltd.. Zinc nitrate hexahydrate (Zn(NO₃)₂·6H₂O) was provided by Alfa Aesar. 2-methylimidazole (2-MeIm) was obtained from Meryer (Shanghai) Chemical Technology Co., Ltd.. [Ru(bpy)₃]Cl₂·6H₂O, acetonitrile (MeCN) and triethanolamine (TEOA) were purchased from Aladdin. All materials were used as received without further purification. Ultrapure water was prepared using the Sartorius, arium mini reinstwasser-system. The CO₂ gas (99.995%) was supplied by Suzhou Jinhong Gas Co. Ltd., and the isotopic ¹³CO₂ gas (99.9%) was purchased from Sigma-Aldrich.

2.2. Synthesis of the materials

Synthesis of ZIF-8, ZIF-67, and Zn/Co-BMZIFs: ZIFs with various Zn/Co mole ratio including 1:0, 5:1, 3:1, 1:1, 1:3, 1:5 and 0:1 were prepared based on previously published procedures.^{26, 34} Typically, the corresponding amount of Zn(NO₃)₂·6H₂O and Co(NO₃)₂·6H₂O (8 mmol in total) were dissolved in 100 mL methanol, and then added into 100 mL methanol containing 30 mmol of the 2-MeIm ligand under sonication for 10 min at room temperature. The obtained solution was further aged at room temperature (RT) for 24 h without stirring. Finally, the obtained precipitates were centrifuged and washed with methanol 3 times and dried in vacuum at 70 °C for overnight. Except for ZIF-8 containing exclusive Zn and ZIF-67 containing only Co, products of bimetallic ZIFs are denoted as BMZIF_{x:y}, where x:y refers to the added mole ratio of the starting materials Zn(NO₃)₂·6H₂O vs. Co(NO₃)₂·6H₂O.

Synthesis of C-ZIF-8, C-ZIF-67 and C-BMZIFs: 50 mg ZIF powder with various Zn/Co mole ratio was annealed at 700 °C for 2 hours in the tube furnace with a heating rate of 1 °C/min under the N₂ (100 mL/min) atmosphere to yield rhombic dodecahedral particles. After annealing, the carbonized ZIF-8 and ZIF-67 are denoted as C-ZIF-8 and C-ZIF-67, respectively. The carbonized BMZIFs with different Zn/Co ratio are denoted as C-BMZIF_{x:y}, where x:y again refers to the added mole ratio of the starting materials, Zn(NO₃)₂·6H₂O and Co(NO₃)₂·6H₂O, used for synthesizing the parent MOF.

2.3. Characterization

The crystal structure was characterized by powder X-ray diffraction (XRD, Bruker D8 Advance with Cu K α radiation ($\lambda=1.54056$ Å)). The surface morphology and micro-structure were observed via a dual-beam electron microscope (SEM, FEI Scios) and a field-emission transmission electron microscope (TEM, FEI TECNAI G2 F20 200 kV) equipped with an energy-dispersive X-ray analyzer (EDX). High-angle annular dark field scanning transmission electron microscopy (HAADF-STEM, Cs-corrected TEM, FEI Titan Themis Cubed G2 300) was used to inspect one of the pyrolyzed samples C-BMZIF_{5:1} for metal dispersion in high resolution. Chemical states of surface elements were probed by X-ray photoelectron spectroscopy (XPS, Thermo Fisher, Escalab 250Xi) using a monochromatic Al K α (1486.6 eV) X-ray source, with all binding energy values calibrated by C 1s = 284.6 eV. Raman spectra were obtained on a confocal laser Raman microscopy (Horiba Jobin Yvon, HR Evolution). Thermal gravimetric analysis (TGA) was performed with EXSTAR

7300 under air with a heating rate of 5 °C/min. N₂ adsorption-desorption isotherms were determined on Micromeritics Tristar II 3020 at 77K. Based on the adsorption branches, the Brunauer-Emmett-Teller (BET) method was used to calculate specific surface area (S_{BET}). Inductively coupled plasma emission spectrometer (ICP) with an OPTIMA 8000 analyzer (PerkinElmer Inc.) was used for elemental analysis of metal ions. Steady-state photoluminescence spectra were recorded on a FluoroMax-4 Spectrofluorometer. ¹H NMR Spectra were obtained on an Agilent NMR system spectrometer (400MHz).

2.4. Photocatalytic test

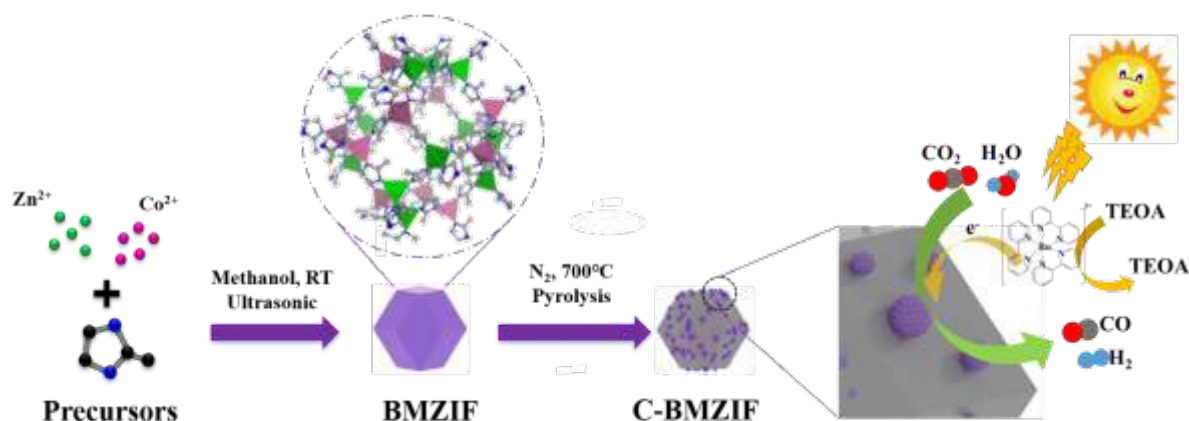
The photocatalytic reduction of CO₂ was carried out in an external irradiation-type reactor (Pyrex glass) with a quartz window on top of the reactor. The reactor is connected to a closed gas-circulation system (Labsolar-6A, Beijing Perfectlight technology Co, Ltd.). Typically, 2 mg of C-BMZIFs catalyst and 40 mg of photosensitizer [Ru(bpy)₃]Cl₂·6H₂O were uniformly dispersed in a solution of TEOA/H₂O/MeCN (2mL/2mL/10mL) in a petri dish with a diameter of 5 cm, and then placed into the reactor, which was cooled by circulating water to maintain the reaction temperature at 4 °C in order to reduce the evaporation rate of MeCN during the photocatalytic process. After the whole system was completely evacuated for 10 minutes to exhaust the air (no O₂ and N₂ is detectable from the gas chromatography), 80 kPa of pure CO₂ gas was injected into the airtight system and kept circulating. A 100 W LED light (PLS-LED 100, 420 nm, Beijing Perfectlight technology Co., Ltd.) was used as the light source, and the illumination distance was kept at 7.5 cm from the sample. The gas products (CO, CH₄, H₂, O₂ and N₂) were analyzed every 1 h by online gas chromatography (GC 2002, Shanghai Kechuang Chromatograph instruments Co., Ltd.) equipped with a thermal conductivity detector (TCD) and a flame ionization detector (FID), using argon as the carrier gas. The quantification of the CO and H₂ was calculated by the calibration curve with a fitting equation obtained using the external standard method. The solution products in the liquid phase were analyzed by ¹H nuclear magnetic resonance spectroscopy (¹H NMR). The isotope

¹³CO₂ experiment was carried out under the same experimental condition and analyzed by mass spectroscopy with an offline injection method, by which 1 mL of the gas in the reactor was extracted and analyzed 10 times before and after the photocatalytic reaction, respectively, and then the difference of average was plotted to obtain the final ¹³C spectrogram. To evaluate the cyclability of the co-catalyst, a partition method was applied to compensate the filtration and transfer loss of the catalyst between each cycle. Specifically, in each cycle we used 2 mg of the C-BMZIF_{1:1} from a total of 20 mg for photocatalysis, and then after each 2 mg cycle, a parallel experiment was performed for the rest of the co-catalyst under the same condition. Afterwards, all of the co-catalysts were mixed together again, and after washing, centrifugation and drying, another 2 mg was taken out for the sequential run.

3. Results and discussion

All ZIF samples were synthesized using metal nitrates and 2-MeIm ligands under sonication at room temperature (Scheme 1). Fig. 1a-c shows the particle morphology of ZIF-8, ZIF-67 and BMZIF_{1:1}, with all three samples exhibiting the similar rhombic dodecahedral shape. However, their size varies significantly. While ZIF-67 has the largest average size about 574 ± 121 nm, those of ZIF-8 and BMZIF_{1:1} are 120 ± 15 and 100 ± 20 nm, respectively. This observation clearly shows that the addition of Zn into ZIF-67 to form bimetallic ZIFs enables dramatically decreasing the size of MOF particles that serve as the scaffold for hosting catalytic active sites.

Despite the difference in coordination chemistry and particle size, PXRD analysis on ZIF-8, ZIF-67, and BMZIF_{1:1}, however, reveals similar diffraction patterns (Fig. 2), indicating they share the same topologic structure. All three samples display the same type-I N₂ adsorption isotherm (Fig. S1a) with close values of specific surface area (BET) being 1431, 1434 and 1382 m²·g⁻¹ for ZIF-8, ZIF-67 and BMZIF_{1:1}, respectively, which are in good agreement with previous literature reports.^{16, 26, 37} TEM images of BMZIF_{1:1} clearly present the well-defined rhombic dodecahedral crystal structure, with elemental mapping from the energy-dispersive X-ray



Scheme. 1 Schematic illustration of the synthesis of C-ZIFs and the role of Co active sites in photocatalysis.

(EDX) spectroscopy showing homogeneously dispersed Zn, Co elements (Fig. S2). Thermogravimetric analysis (TGA) reveals a better thermal stability of ZIF-8, sequentially followed by the BMZIF_{1:1} and ZIF-67 (Fig. S1b). As for the solvent stability, a similar trend was observed for these three samples in a mixed solvent containing water, triethanolamine and methyl cyanide, which has been typically used in [Ru(bpy)₃]²⁺ mediated photocatalysis. In fact, ZIF-67 is so unstable that after overnight the purple color of the solution faded severely (Fig. S3).

As a means to improve the stability while still maintaining the MOF scaffold, all ZIF samples were carbonized at 700 °C for 2 h under the N₂ atmosphere in a tube furnace. This annealing temperature was chosen based on below considerations: First, both TGA curves (Fig. S1b) and Raman spectra (Fig. S4) indicate at 700 °C all ZIF samples are sufficiently carbonized. Second, ZIFs annealed at 700 °C are able to maintain their rhombic dodecahedral structure even after intensive sonication (Fig. 1d-f, required for their homogeneous dispersion in the photocatalytic system), whereas those annealed at higher temperature (for example at 900 °C) will collapse and break into small debris (Fig. S5). Third, a lower annealing temperature can be used to avoid the severe Oswald ripening of nanoparticles, which is beneficial for the photocatalytic

efficiency. BET analysis on the carbonized ZIFs at 700 °C (Fig. S6) revealed drastically decreased specific surface areas, with the measured values of 166, 68, and 85 m²·g⁻¹ for C-ZIF-8, C-ZIF-67 and C-BMZIF_{1:1}, respectively. The decrease in surface area indicates the pore structure of the original ZIFs is diminished after carbonization.

SEM images (Fig. 1d-f) show the carbonized C-ZIF-8, C-ZIF-67 and C-BMZIF_{1:1} at 700 °C inherit the original MOF morphology with slightly shrunken surfaces. While the surface of C-ZIF-8 seems smooth, a large number of small nanoparticles can be visualized on the surface of both C-ZIF-67 and C-BMZIF_{1:1}, and the particle size observed on C-ZIF-67 is significantly larger. TEM images (Fig. 1g-i, Fig. S7) further reveals more nanoparticles with larger size (11.8 ± 3.3 nm) in C-ZIF-67, whereas those in C-BMZIF_{1:1} are much less and smaller (4.1 ± 2.1 nm). As there are no nanoparticles seen on C-ZIF-8 from both SEM and TEM images, those observed on C-ZIF-67 and C-BMZIF_{1:1} must be agglomerated Co nanoparticles, which is further evidenced by elemental mapping from the SEM-EDX characterization (Fig. S8). Besides, the majority of the Co nanoparticles in C-ZIF-67 are localized at the center of the MOF dodecahedron (Fig. 1h, Fig. S7), whereas those in C-BMZIF_{1:1} appear more scattered (Fig. 1i). Therefore, with the incorporation of

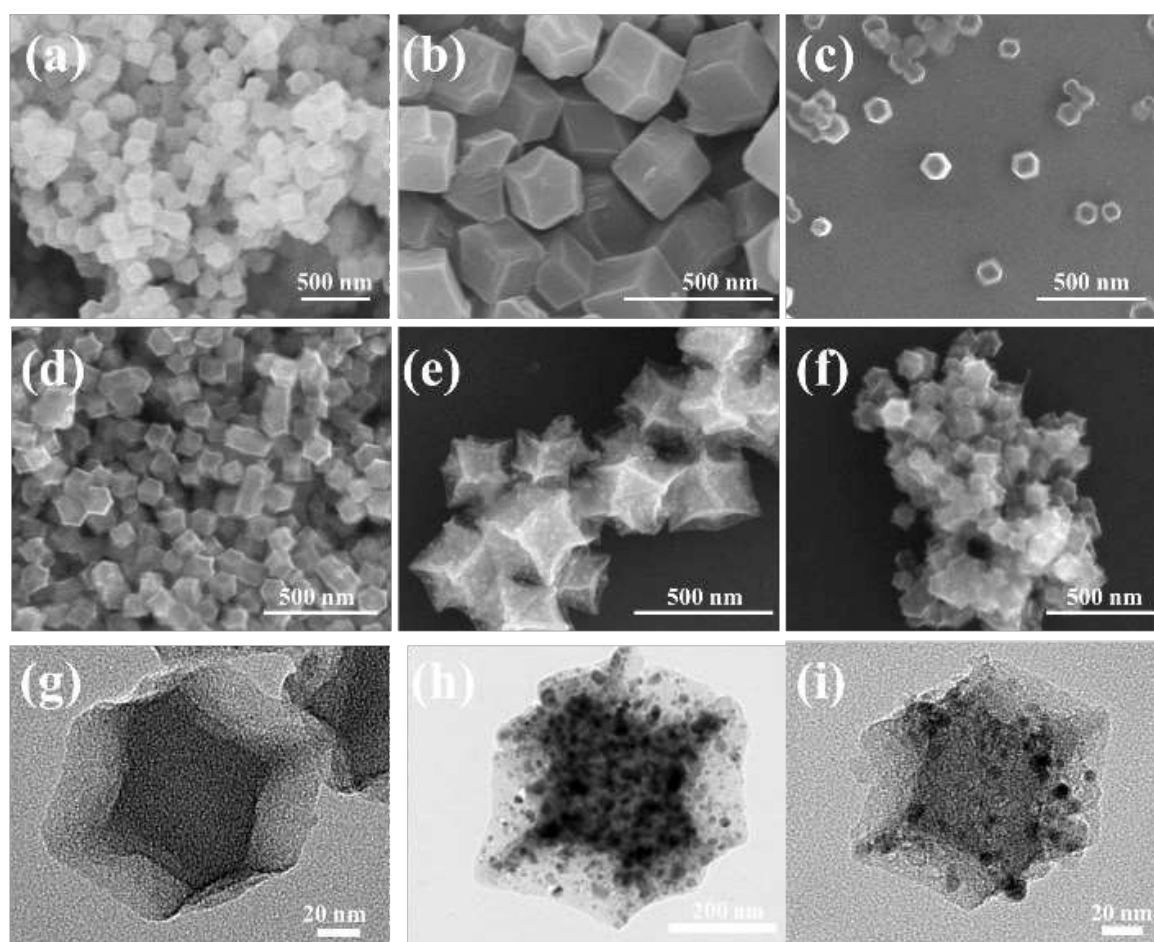


Fig. 1 SEM images showing the morphology of (a) ZIF-8, (b) ZIF-67, (c) BMZIF_{1:1} before carbonization, and (d) C-ZIF-8, (e) C-ZIF-67, (f) C-BMZIF_{1:1} after carbonization. TEM images showing the Co particle size and distribution after carbonization on (g) C-ZIF-8, (h) C-ZIF-67 and (i) C-BMZIF_{1:1} at 700 °C.

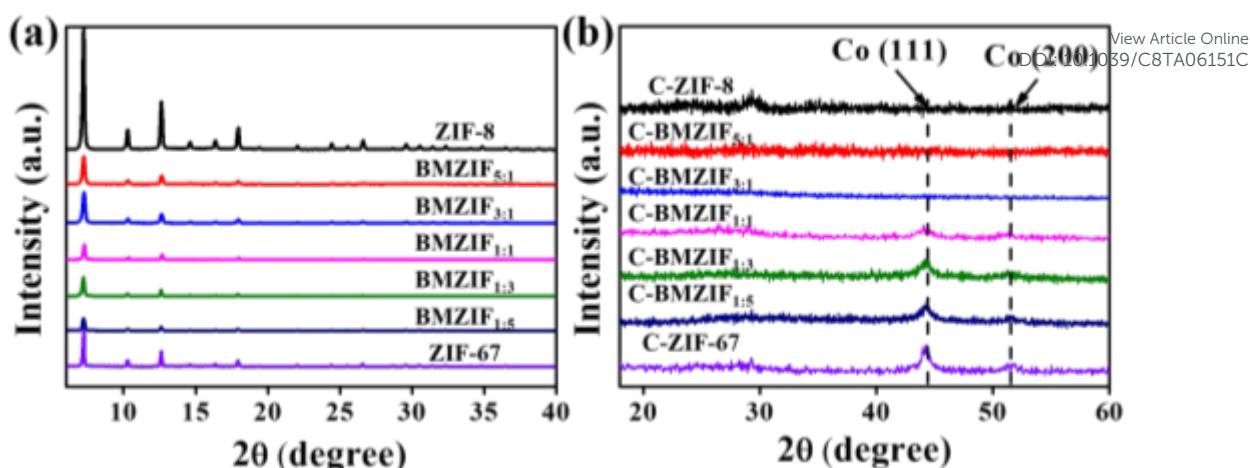


Fig. 2 PXRD of (a) BMZIFs and (b) C-BMZIFs with different Zn/Co ratios.

Zn into Co-ZIF-67 to form bimetallic ZIFs, not only the MOF size, but also the distribution and size of Co active sites formed upon carbonization can be regulated.

Following the lead, next we systematically varied the Zn/Co ratio in the synthesized ZIFs and carefully examined the size evolution of MOF particles and Co active sites upon carbonization. Including the ZIF-8 and ZIF-67, a total of 7 Zn/Co ratios were examined. The smallest MOF particle size was observed on BMZIF_{3:1}, with the average of 100 ± 20 nm and even smaller than that of ZIF-8 (see Fig. S9, S10 for the trend of particle size change with the Zn/Co ratio). The actual Co content and Zn/Co ratio in all BMZIFs were quantified by EDX (Table S1, S2), showing the mass percentages of Co are actually lower than the predicted values based on the raw material stoichiometry. Taking the BMZIF_{5:1} as an example, the measured Co content of 1.16% is significantly lower than the theoretical value of 4.34% calculated based on the reactant ratio, indicating that the actual Zn/Co ratio in the BMZIFs is influenced by both the reactant concentration and the K_{sp} of the final products. Consequently, one will always need to perform elemental analysis to quantify the actual Co content in the BMZIFs, which is confirmed by both EDX and ICP-AES in the current study, showing fairly consistent values with each other (Table S1).

After carbonization, both SEM and TEM characterizations (Fig. 1, 3 and S11) show that Co nanoparticles are formed on all C-BMZIFs except for C-BMZIF_{5:1}, which exhibit almost no difference from C-ZIF-8. The lack of nanoparticles on C-BMZIF_{5:1} was further confirmed by HRTEM, HAADF-STEM and the corresponding EDS images acquired by a Cs-corrected TEM (Fig. S12), showing all elements including Zn, Co are homogeneously dispersed in the sample. On C-BMZIF_{3:1}, nanoparticles with extremely fine size of 2.3 ± 0.65 nm are visible across the whole sample with sporadic agglomerated ones. Beyond that, both the amount and size of Co nanoparticles monotonically increase with the decreasing Zn/Co ratio (Fig. S13). The carbonized C-BMZIFs with various Zn/Co ratios were further characterized by XRD to illustrate the structural evolution. As shown in Fig. 2b, after the thermal treatment at 700 °C, the original diffraction pattern characteristic of ZIFs (Fig. 2a) completely disappears, accompanied with the monotonical evolution of Co (111) and (200) peaks at the 2θ of 44.2° and 51.6° (PDF # 15-0806) with the decreasing of Zn/Co ratio. Surprisingly, there are no

Co peaks detectable on both C-BMZIF_{5:1} and C-BMZIF_{3:1}, suggesting that the Co nanoparticles, if exist, are too small or less to be probed by XRD. In addition, no peaks of Zn are visible across all spectra, confirming their existence in the coordinated state and no agglomeration of Zn nanoparticles.

XPS survey spectra reveal the presence of C, N, Zn and Co elements in all C-BMZIFs (Fig. S14). The high-resolution C 1s spectra (Fig. S15) illustrate that the dominant carbon species after pyrolysis are the sp^2 -hybridized carbon of C=C bonds (~ 284.8 eV), C=N bonds (~ 285.6 eV) and sp^3 -hybridized carbon of C-N bonds (~ 286.7 eV), and the composition of graphitic carbon increases with the increasing Co content.^{38, 39} For N 1s (Fig. S16), XPS shows the major species include pyridinic (~ 398.7 eV), pyrrolic (~ 399.9 eV) and graphitic (~ 401.1 eV) nitrogen, with an overall increase of the graphitic nitrogen with the increasing Co content.^{40, 41} For all carbonized samples excluding C-ZIF-67, Zn 2p_{3/2} and Zn 2p_{1/2} peaks can be detected and are located at ~ 1021.9 eV and ~ 1044.8 eV, respectively, corresponding to the coordinated state of Zn^{2+} (Fig. S17).^{30, 35, 42, 43}

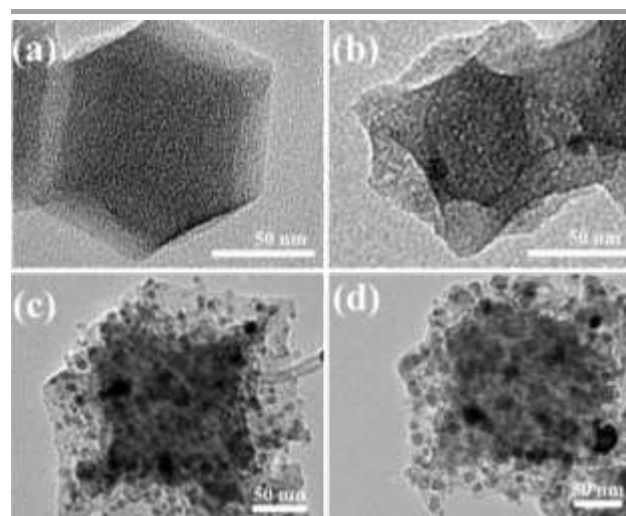


Fig. 3 TEM images of C-BMZIFs with the Zn/Co ratio of (a) 5:1, (b) 3:1, (c) 1:3, (d) 1:5. While no distinct Co particles is visible on C-BMZIF_{5:1}, the size of Co particles increases with the decreasing Zn/Co ratio for the other samples.

More importantly, XPS analysis of Co $2p_{3/2}$ and Co $2p_{1/2}$ reveals prominent peaks of Co⁰ at 778.5 and 793.6 eV, respectively, on C-BMZIFs when the Zn/Co ratio is above 3:1, whereas on C-BMZIF_{5:1} they are barely detectable (Fig. 4). The absence of the Co⁰ species indicates little metallic Co particles in C-BMZIF_{5:1}, in resonance with the above TEM and XRD analysis. Co²⁺ is the other major cobalt species existing across all Co-containing samples, and its intensity ratio to Co⁰ decreases with the decreasing Zn/Co ratio. An exception, however, is the C-ZIF-67, in which a relatively low level of Co⁰ (compared to Co²⁺) is observed. This is likely due to the much larger size of C-ZIF-67, and the fact that the majority of Co nanoparticles are localized at the center of the polyhedron, as XPS is a surface-sensitive technique. Previous studies have also shown that the agglomeration of metal nanoparticles can be effectively inhibited by the largely dispersed Zn in bimetallic ZIFs, even resulting in atomic metal sites with various nitrogen coordination.³² This could be the case of C-BMZIF_{5:1} in the current study, as HR-TEM, HAADF-STEM, XRD, and XPS all failed to detect any metallic cobalt particles. However, to further prove this, more quantitative characterizations such as Extended X-ray absorption fine structure (EXAFS) are needed. Nevertheless, our investigations unambiguously demonstrate that varying the Zn/Co ratio in bimetallic ZIFs allows regulating the size and distribution of Co active sites on the carbonized MOF scaffold.

The catalytic potency of all carbonized ZIFs was evaluated in a hybrid photocatalytic system, using [Ru(bpy)₃]²⁺ as the photosensitizer and TEOA as the electron donor. In a typical experiment, a 14 mL solution of MeCN/H₂O/TEOA (10:2:2, v/v/v) containing 2 mg of the co-catalyst and 40 mg of [Ru(bpy)₃]Cl₂·6H₂O

were illuminated by a 100 W LED light ($\lambda = 420$ nm) for a duration of 3 hours. Under these conditions, in all experiments CO and H₂ were detected by gas chromatography (GC) as the only reduction products (Fig. S18a), and no other soluble products such as formate were found by the ¹H nuclear magnetic resonance spectroscopy (¹HNMR, Fig. S18b).^{12, 44} Fig. 5a and 5b present the evolution of CO and H₂, respectively, within the 3-hour illumination time for C-ZIF-8, C-BMZIF_{1:1}, and C-ZIF-67. Among these three samples, C-BMZIF_{1:1} produced the highest amount of CO of 47.5 μ mol, whereas C-ZIF-67 had the highest H₂ evolution of 56.4 μ mol. C-ZIF-8 barely exhibits any catalytic reactivity, and shows no distinguishable difference in both CO and H₂ production from the control experiment without any co-catalysts (Fig. S19). This confirms that Co sites in both C-BMZIFs and C-ZIF-67 are solely responsible for their catalytic behaviors.

Extending the photoreaction time beyond 3 hours (Fig. 5c), we start to see the rate of CO evolution slows down, possibly due to the deactivation of the photosensitizer. It is well known that in such hybrid photocatalytic systems the deactivation of photoabsorbers poses a common issue,^{3, 45} but the deactivation of the co-catalyst also cannot be ruled out. Therefore, in order to confirm whether the slow-down of CO evolution is caused by the deactivation of the co-catalyst, we performed two stability tests. In the first relay test, at the end of the 6th hour, an equal amount of photosensitizer [Ru(bpy)₃]²⁺ was replenished into the photocatalytic system and the reaction was found resumed (Fig. 5c). In the second cycling test, we recycled the C-BMZIF_{1:1} co-catalyst by filtration (see the photocatalytic test for experimental details) and examined its cycling stability (Fig. 5d). A total of 3 consecutive cycles were carried out using the same co-

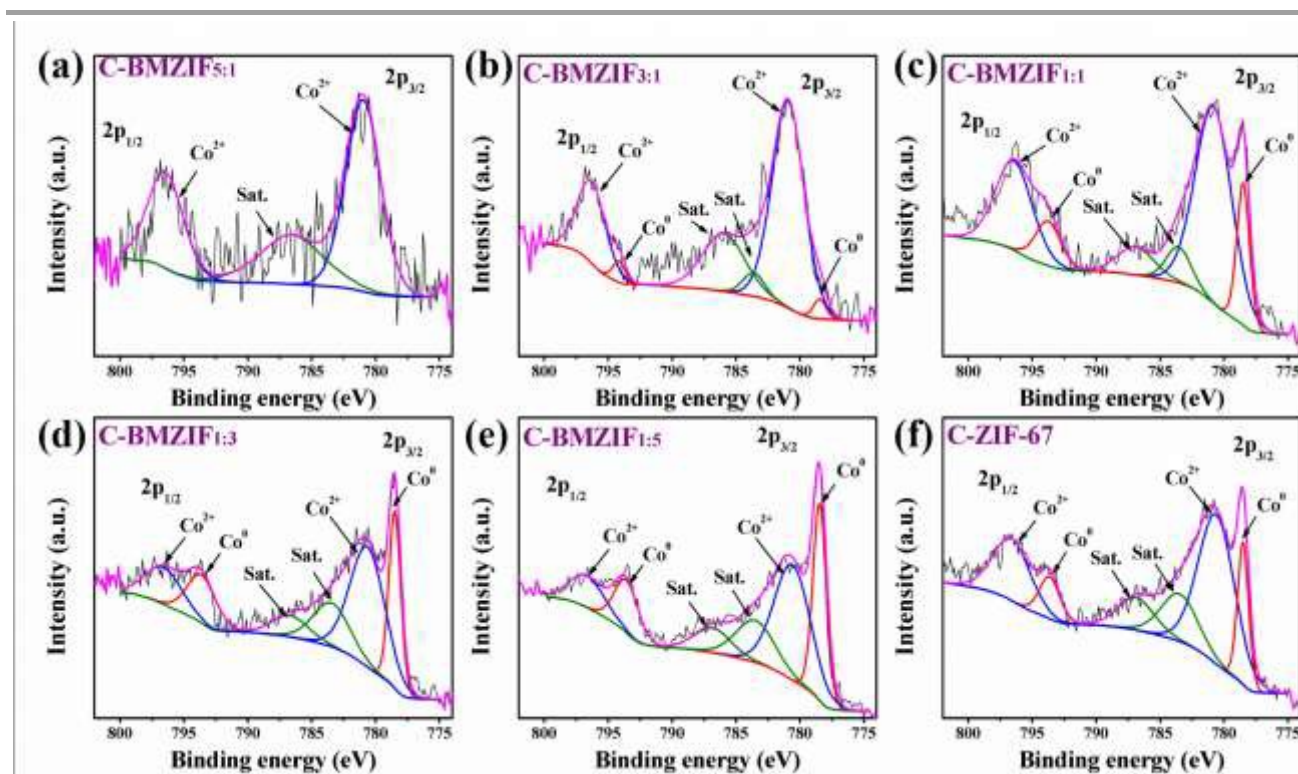


Fig. 4 XPS Co 2p spectra of (a) C-BMZIF_{5:1}, (b) C-BMZIF_{3:1}, (c) C-BMZIF_{1:1}, (d) C-BMZIF_{1:3}, (e) C-BMZIF_{1:5}, (f) C-ZIF-67. The evolution of Co⁰ species is distinguishable on all samples with the Zn/Co ratio above 5:1.

catalyst, showing no sign of performance decay. What's more, SEM and PXRD characterizations were performed on the recycled C-BMZIF_{1:1} after photocatalysis to verify their structural integrity (Fig. S20), and both analysis reveal no structural change of the co-catalyst throughout all conducted experimental cycles. These results clearly demonstrate that C-BMZIFs as the co-catalyst in our hybrid photocatalytic system possesses excellent stability and durability, whereas the deactivation of the photosensitizer is the limiting factor for extended CO₂ RR.

To justify the role of the co-catalyst in our hybrid photocatalytic system, various control experiments were carried out under different conditions (Fig. S19). First, without using the co-catalyst, there was only 6.1 μmol CO and 4.6 μmol H₂ produced in 3 hours, whereas the aforementioned complete photocatalytic system containing 2 mg C-BMZIF_{1:1} and 40 mg [Ru(bpy)₃]²⁺ produced 47.5 μmol CO and 47.4 μmol H₂. Second, when there was no photosensitizer used in the photocatalytic system, neither CO nor H₂ was detected, indicating C-BMZIF_{1:1} alone is not sufficient to trigger the catalytic reaction, and the electrons for CO₂ reduction come from photoelectrons generated by the photosensitizer. This point of view is further confirmed by photoluminescence (PL) characterizations (Fig. S21a), in which the characteristic emission peak of the photosensitizer at about 620 nm monotonically decreases with the addition of C-BMZIF_{1:1}. In addition, the flat band potential of C-BMZIF_{1:1} is measured ca. -0.76

V (vs. NHE) based on the Mott-Schottky analysis (Fig. S21b), lower than the redox potential of E([Ru(bpy)₃]³⁺/[Ru(bpy)₃]²⁺) = 0.87 V (vs. NHE) and higher than that of E(CO₂/CO) = -0.53 V (vs. NHE).⁴⁶⁻⁴⁸ Both the PL and Mott-Schottky analysis indicate C-BMZIF_{1:1} are capable of mediating the electron transfer from the redox couple [Ru(bpy)₃]³⁺/[Ru(bpy)₃]²⁺ to CO₂/CO. Third, when the irradiation was cut from the experiments, there was also no detectable CO and H₂, confirming the reaction is indeed photocatalyzed. Fourth, when there was no supply of CO₂ with all other conditions maintained the same, again no CO was detected except for H₂ (18.4 μmol), indicating that the above produced CO is exclusively from CO₂. Moreover, isotopic ¹³CO₂ experiments were conducted under identical conditions with the reduction products analyzed by GC and mass spectra. A strong peak at *m/z* = 29 (Fig. S22), assignable to ¹³CO, is present in the mass spectra, proving the carbon source of CO does indeed come from the CO₂, rather than other organic reagents such as TEOA. Lastly, the supernatant after photocatalysis was collected by filtration for ICP analysis of possible Co²⁺ leaching, showing no Co species within the detection limit. Moreover, photocatalytic CO₂ reduction was carried out using the filtered supernatant with fresh [Ru(bpy)₃]²⁺ and TEOA, exhibiting no distinct CO and H₂ evolution after 3 h illumination (Fig. S19). These experiments confirm that the photocatalytic reaction in the current study is a heterogeneous catalytic process.

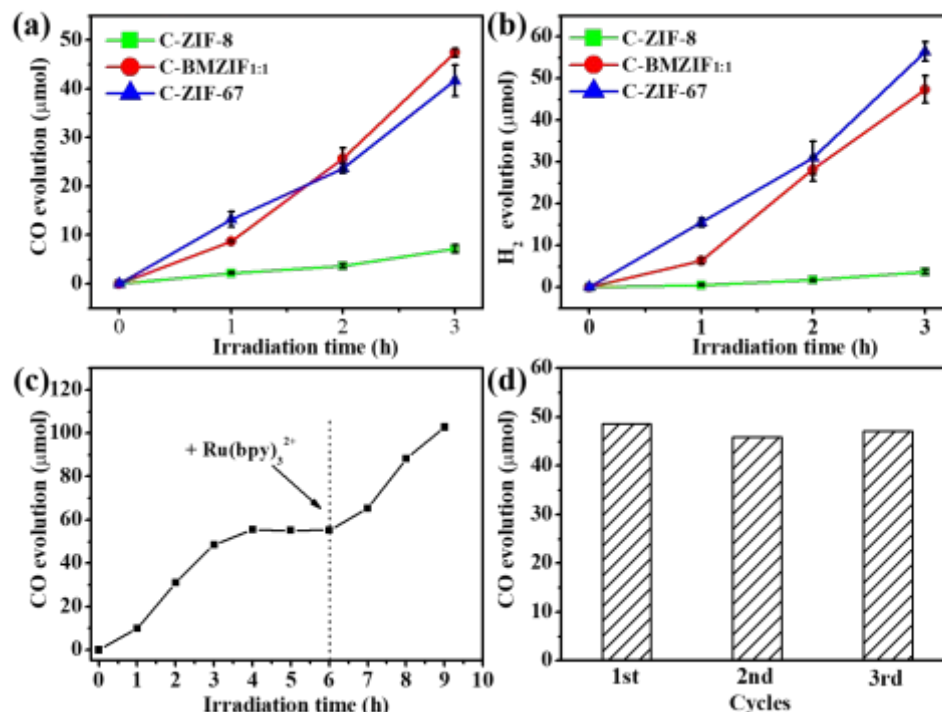


Fig. 5 Photocatalytic performance of C-ZIF-8, C-ZIF-67 and C-BMZIF_{1:1}. (a) CO and (b) H₂ evolution vs illumination time in the MeCN/H₂O/TEOA solution (14 mL 10:2:2 v/v/v), containing 40 mg [Ru(bpy)₃]Cl₂·6H₂O and 2 mg co-catalysts; (c) the relay stability and (d) the cycling stability test for C-BMZIF_{1:1}.

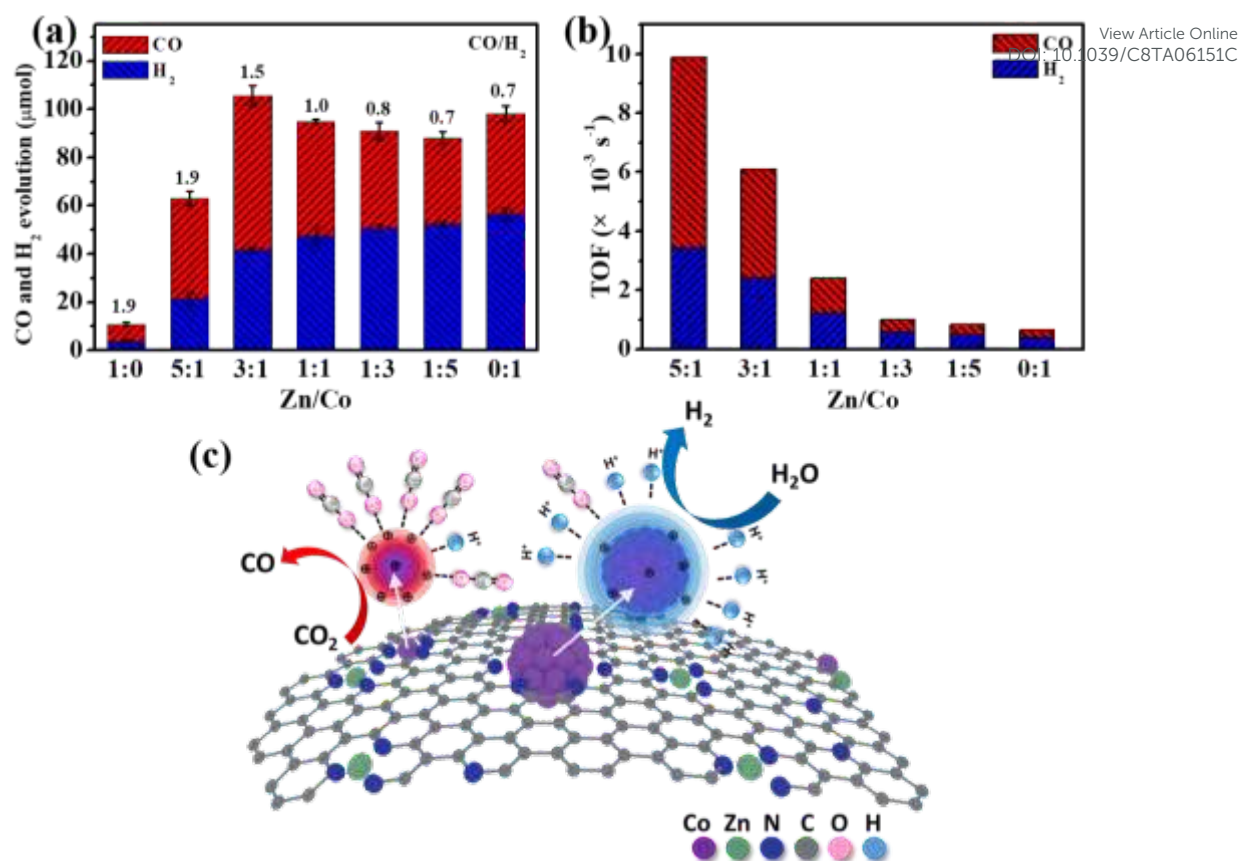


Fig. 6 Histograms for comparing the CO and H₂ evolution rate and turnover frequencies. (a) The total evolution of CO and H₂ within the 3 h photocatalytic reaction for C-BMZIFs with various Zn/Co ratios. (b) the corresponding TOFs based on the mass percentage of Co quantified by EDX. (c) Proposed selectivity cause of the photocatalytic CO₂ reduction to syngas by C-BMZIFs.

To further interrogate the correlation of the size of Co active sites with their catalytic activity and product selectivity, systematic photocatalytic experiments of CO₂ RR were carried out using C-BMZIFs with different ratio of Zn/Co as the co-catalysts. As shown in Fig. 6a, without Co the C-ZIF-8 exhibits no activity and both CO and H₂ evolution are similar to those acquired without adding any co-catalysts (Fig. S19). Then, with the increasing of Co ratio in the bimetallic ZIFs, the H₂ evolution increases monotonically. The CO evolution, however, does not correlate well with the Co content and a maximal value is observed for C-BMZIF_{3:1}. Based on the statistics of Co particle size distribution (Fig. S13), it is clear that the evolution rate of H₂ is higher on larger Co particles, whereas that of CO is more favored on Co sites with small particle size. Accordingly, the CO/H₂ ratio in the produced syngas exhibits an overall trend of descending with the decreasing Zn/Co ratio in the bimetallic ZIFs. In addition, a rough comparison can be made on the lower bound of the turnover frequency (TOF) for both CO₂ reduction and H₂ evolution, assuming all Co elements detected by EDX in the co-catalyst participate to the conversion reactions (Table S3). Fig. 6b summarizes the thus obtained TOFs on both CO and H₂ evolution for C-BMZIFs with various Zn/Co ratios. On one hand, C-BMZIF_{5:1} demonstrates the highest activities for both H₂ and CO evolution, with a high TOF of $3.4 \times 10^{-3} \text{ s}^{-1}$ for HER and $6.5 \times 10^{-3} \text{ s}^{-1}$ for CO₂ RR, respectively. Notably, the TOF of CO₂ RR for C-BMZIF_{5:1} is 23-fold higher than that for C-ZIF-67 ($0.28 \times 10^{-3} \text{ s}^{-1}$),

which is likely due to the mono-dispersion of Co active sites within the carbon matrix. On the other hand, C-BMZIF_{3:1} gives the highest yield of CO, $1.1 \times 10^4 \mu\text{mol g}^{-1} \text{ h}^{-1}$, as a result of the optimal balance between the quantity of active sites and the activity of each individual site. In comparison to previous reports of photocatalytic CO₂ reduction using ZIF-67 as the co-catalyst and [Ru(bpy)₃]²⁺ as the photosensitizer, the catalytic activities revealed in this study for carbonized BMZIFs are comparable to those obtained for ZIF-67, ranging from $3.89 \times 10^3 \mu\text{mol g}^{-1} \text{ h}^{-1}$ to $5.9 \times 10^4 \mu\text{mol g}^{-1} \text{ h}^{-1}$.¹⁰ However, when taking into account the mass percentage of Co in the co-catalyst and the stability of carbonized materials, C-BMZIFs exhibit some intrinsic advantages. In the hybrid photocatalytic system of this study, the catalytic activity and product selectivity are a comprehensive outcome of various contributing factors. First, the size of the Co active sites constitutes the major influential factor on the product selectivity by promoting the CO evolution rate on smaller Co particles. Second, while higher Co content is in favor of the overall gas production, this enhancement effect is constrained by the agglomeration of Co particles when less Zn is contained in the bimetallic ZIFs. As a result, although the Co content of C-ZIF-67 is over 20 times higher than that of C-BMZIF_{5:1}, the total product yield (including both H₂ and CO) of the former is only 1.5 times of the latter. Therefore, there exists an optimal Zn/Co ratio that balance both catalytic activity and production yield. Third, the particle size of MOFs that serve as the scaffold for hosting the Co active sites also

plays an important role by affecting their spatial distribution, as well as the specific surface area for reaction kinetics. Consequently, the highest product yield with high CO/H₂ ratio was obtained by C-BMZIF_{3:1}, in which both of the size and exposed quantity of Co active sites are balanced to an optimal level.

Further regarding the photocatalytic process and product selectivity, we were able to propose a reaction mechanism based on the above observations and discussions. As illustrated in Scheme 1, upon illumination the photosensitizer [Ru(bpy)₃]²⁺ is excited to [Ru(bpy)₃]^{2+*}, which is a highly potent electron donor. Then, at elevated energy levels, the photoexcited electron of [Ru(bpy)₃]^{2+*} could be readily delocalized from its π* orbital and further transferred to the Co active sites.^{47,49} Simultaneously, a hole will be left in the HOMO orbital of the sensitizer, accepting an electron from the readily available TEOA with the sensitizer acting as an oxidant. The highly reductive electrons transferred to the Co active sites will further interact with the surface-absorbed proton and CO₂ species to produce H₂ and CO through a two-electron transfer process. Moreover, the observed size-dependent product selectivity can be rationalized by the following explanation and Fig. 6c. Due to the surrounding nitrogen coordination, the surface of Co particles are likely positively charged, especially when the particle size is small (with a higher positive charge density). Thus, the CO₂ absorption on the co-catalyst surface is mainly through the Co-O-C=O linkage, which has been known more favorable for the subsequent CO formation.⁵⁰⁻⁵¹ Otherwise, if CO₂ is absorbed on the catalyst surface through the Co-C-O linkage, which is less likely in the current case due to the positively charged metal surface, formic acid can be the reduction product. In comparison to small Co particles, the lower density of positive charges on the larger Co particles favors the adsorption of H⁺, which are more repelled by the more positively charged small Co particles (favoring the Co-O-C=O linkage instead). Thus, higher selectivity towards CO production can be witnessed for the Co active sites with smaller size.

4. Conclusion

In summary, a series of C-BMZIFs catalysts with the inherited rhombic dodecahedral structure were successfully synthesized through the pyrolysis of bimetallic Zn/Co ZIFs at 700 °C under an inert N₂ atmosphere. The presence of Zn and reduced content of Co in the framework can effectively inhibit the aggregation of Co during pyrolysis, and therefore the size of the resulted Co active sites can be regulated by adjusting the Zn/Co ratio. When used as the co-catalyst in photocatalytic CO₂ conversion, the C-BMZIF with a Zn/Co ratio of 5:1 demonstrated the highest TOF of CO₂ RR, 23-fold larger than that of C-ZIF-67, whereas the C-BMZIF_{3:1} gave the highest CO yield, owing to the optimal balance between the quantity of active sites and the activity of individual sites. Moreover, it was found while the evolution rate of H₂ is higher on larger Co particles, that of CO is more favored on Co sites with smaller size. Consequently, by varying the Zn/Co ratio in the BMZIFs and thus regulating the exposure of Co active sites in the C-BMZIFs, the CO/H₂ ratio in the produced syngas can be tuned from 1.9 – 0.7. The reaction mechanism and selectivity cause was explained in details considering the energy flow and particle charge. This work sheds new light on the design of non-noble-metal photocatalysts for

efficient CO₂ RR and offers an alternative solution for photocatalytic syngas production with tunable CO/H₂ ratio. DOI: 10.1039/C8TA06151C

Conflicts of interest

There are no conflicts to declare.

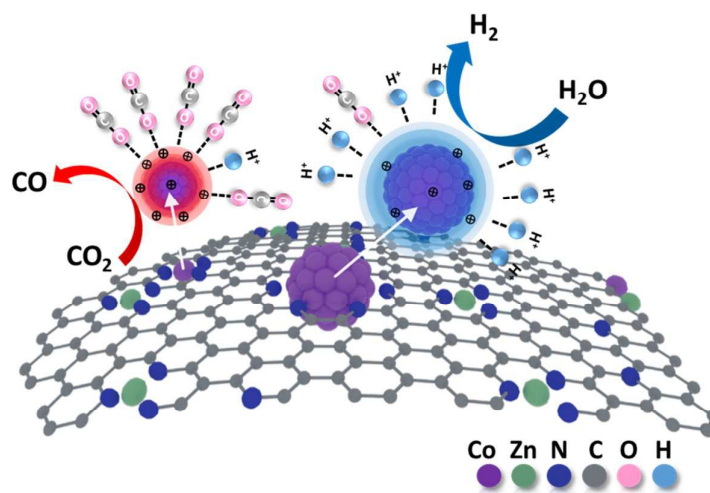
Acknowledgements

This work was supported by the 1000 Young Talents Program of China, Natural Science Foundation of China (No. 21701118), Natural Science Foundation of Jiangsu Province (No. K20161209 and No. BK20160323) and the Key Technology Initiative of Suzhou Municipal Science and Technology Bureau (SYG201748). We also extend our sincere appreciation to the support by Suzhou Key Laboratory for Advanced Carbon Materials and Wearable Energy Technologies, Suzhou 215006, China.

References

- S. Rasul, D. H. Anjum, A. Jedidi, Y. Minenkov, L. Cavallo and K. Takanebe, *Angew. Chem. Int. Ed.*, 2015, **54**, 2146-2150.
- Q. Cheng, K. Mao, L. Ma, L. Yang, L. Zou, Z. Zou, Z. Hu and H. Yang, *ACS Energy Lett.*, 2018, **3**, 1205-1211.
- J. Qin, S. Wang and X. Wang, *Appl. Catal. B: Environ.*, 2017, **209**, 476-482.
- W. Tu, Y. Zhou and Z. Zou, *Adv. Mater.*, 2014, **26**, 4607-4626.
- J. Wu, Y. Huang, W. Ye and Y. Li, *Adv. Sci.* 2017, **4**, 1700194(1)-1700194(29).
- Y. Li, H. Xu, S. Ouyang and J. Ye, *Phys. Chem. Chem. Phys.*, 2016, **18**, 7563-7572.
- Y. Zhang, L. Li, Q. Han, L. Tang, X. Chen, J. Hu, Z. Li, Y. Zhou, J. Liu and Z. Zou, *Chemphyschem*, 2017, **18**, 3240-3244.
- T. N. Huan, N. Ranjbar, G. Rousse, M. Sougrati, A. Zitolo, V. Mougel, F. Jaouen and M. Fontecave, *ACS Catal.*, 2017, **7**, 1520-1525.
- K. P. Kuhl, T. Hatsukade, E. R. Cave, D. N. Abram, J. Kibsgaard and T. F. Jaramillo, *J. Am. Chem. Soc.*, 2014, **136**, 14107-14113.
- M. Wang, J. Liu, C. Guo, X. Gao, C. Gong, Y. Wang, B. Liu, X. Li, G. G. Gurzadyan and L. Sun, *J. Mater. Chem. A.*, 2018, **6**, 4768-4775.
- Y. Wang, N. Y. Huang, J. Q. Shen, P. Q. Liao, X. M. Chen and J. P. Zhang, *J. Am. Chem. Soc.*, 2018, **140**, 38-41.
- S. Wang, W. Yao, J. Lin, Z. Ding and X. Wang, *Angew. Chem. Int. Ed.*, 2014, **53**, 1034-1038.
- S. Wang, B. Y. Guan and X. W. Lou, *Energy Environ. Sci.*, 2018, **11**, 306-310.
- K. Niu, Y. Xu, H. Wang, R. Ye, H. L. Xin, F. Lin, C. Tian, Y. Lum, K. C. Bustillo, M. M. Doeff, M. T. M. Koper, J. Ager, R. Xu and H. Zheng, *Sci. Adv.*, 2017, **3**, e1700921.
- M. Jiang, Y. Gao, Z. Wang and Z. Ding, *Appl. Catal. B: Environ.*, 2016, **198**, 180-188.
- J. W. Maina, C. Pozo-Gonzalo, L. X. Kong, J. Schutz, M. Hill and L. F. Dumee, *Mater. Horiz.*, 2017, **4**, 345-361.
- S. J. Guo, S. Q. Zhao, X. Q. Wu, H. Li, Y. J. Zhou, C. Zhu, N. J. Yang, X. Jiang, J. Gao, L. Bai, Y. Liu, Y. Lifshitz, S. T. Lee and Z. H. Kang, *Nat. Commun.*, 2017, **8**, 1828-1837.
- W. Sheng, S. Kattel, S. Yao, B. Yan, Z. Liang, C. J. Hawxhurst, Q. Wu and J. G. Chen, *Energy Environ. Sci.*, 2017, **10**, 1180-1185.
- F. Marques Mota, D. L. T. Nguyen, J.-E. Lee, H. Piao, J.-H. Choy, Y. J. Hwang and D. H. Kim, *ACS Catal.*, 2018, **8**, 4364-

- 4374.
- 20 V. R. Calderone, N. R. Shiju, D. Curulla-Ferré, S. Chambrey, A. Khodakov, A. Rose, J. Thiessen and D. G. Rothenberg, *Angew. Chem. Int. Ed.*, 2013, **125**, 4493-4497.
 - 21 A. D. Klerk, *Energy Environ. Sci.*, 2011, **4**, 1177-1205.
 - 22 D. Sun, Y. Gao, J. Fu, X. Zeng, Z. Chen and Z. Li, *Chem. Commun.*, 2015, **51**, 2645-2648.
 - 23 X. He, Z. Gan, S. Fisenko, D. Wang, H. M. El-Kaderi and W. N. Wang, *ACS Appl. Mater. Inter.*, 2017, **9**, 9688-9698.
 - 24 Y. Lee, S. Kim, J. K. Kang and S. M. Cohen, *Chem. Commun.*, 2015, **51**, 5735-5738.
 - 25 G. X. Zhao, X. B. Huang, X. X. Wang and X. K. Wang, *J. Mater. Chem. A.*, 2017, **5**, 21625-21649.
 - 26 Y. Z. Chen, C. Wang, Z. Y. Wu, Y. Xiong, Q. Xu, S. H. Yu and H. L. Jiang, *Adv. Mater.*, 2015, **27**, 5010-5016.
 - 27 Y. Chen, D. Wang, X. Deng and Z. Li, *Catal. Sci. Technol.*, 2017, **7**, 4893-4904.
 - 28 K. Shen, X. Chen, J. Chen and Y. Li, *ACS Catal.*, 2016, **6**, 5887-5903.
 - 29 Y.-Z. Chen, R. Zhang, L. Jiao and H.-L. Jiang, *Coord. Chem. Rev.*, 2018, **362**, 1-23.
 - 30 P. Yin, T. Yao, Y. Wu, L. Zheng, Y. Lin, W. Liu, H. Ju, J. Zhu, X. Hong, Z. Deng, G. Zhou, S. Wei and Y. Li, *Angew. Chem. Int. Ed.*, 2016, **55**, 10800-10805.
 - 31 T. A. Wezendonk, V. P. Santos, M. A. Nasalevich, Q. S. E. Warringa, A. I. Dugulan, A. Chojecki, A. C. J. Koeken, M. Ruitenbeek, G. Meima, H.-U. Islam, G. Sankar, M. Makkee, F. Kapteijn and J. Gascon, *ACS Catal.*, 2016, **6**, 3236-3247.
 - 32 X. Wang, Z. Chen, X. Zhao, T. Yao, W. Chen, R. You, C. Zhao, G. Wu, J. Wang, W. Huang, J. Yang, X. Hong, S. Wei, Y. Wu and Y. Li, *Angew. Chem. Int. Ed.*, 2018, **57**, 1944-1948.
 - 33 Y. Pan, R. Lin, Y. Chen, S. Liu, W. Zhu, X. Cao, W. Chen, K. Wu, W. C. Cheong, Y. Wang, L. Zheng, J. Luo, Y. Lin, Y. Liu, C. Liu, J. Li, Q. Lu, X. Chen, D. Wang, Q. Peng, C. Chen and Y. Li, *J. Am. Chem. Soc.*, 2018, **140**, 4218-4221.
 - 34 C. Zhao, X. Dai, T. Yao, W. Chen, X. Wang, J. Wang, J. Yang, S. Wei, Y. Wu and Y. Li, *J. Am. Chem. Soc.*, 2017, **139**, 8078-8081.
 - 35 C. Yan, H. Li, Y. Ye, H. Wu, F. Cai, R. Si, J. Xiao, S. Miao, S. Xie and F. Yang, *Energy Environ. Sci.*, 2018, **11**, 1204-1210.
 - 36 S. Acharya, S. Mansingh and K. M. Parida, *Inorg. Chem. Front.*, 2017, **4**, 1022-1032.
 - 37 J. Cravillon, R. Nayuk, S. Springer, A. Feldhoff, K. Huber and M. Wiebcke, *Chem. Mater.*, 2011, **23**, 2130-2141.
 - 38 Z. Wang, S. Peng, Y. Hu, L. Li, T. Yan, G. Yang, D. Ji, M. Srinivasan, Z. Pan and S. Ramakrishna, *J. Mater. Chem. A.*, 2017, **5**, 4949-4961.
 - 39 P. Yin, T. Yao, Y. Wu, L. Zheng, Y. Lin, W. Liu, H. Ju, J. Zhu, X. Hong, Z. Deng, G. Zhou, S. Wei and Y. Li, *Angew. Chem. Int. Ed.*, 2016, **55**, 10800-10805.
 - 40 J. Wei, Y. Hu, Y. Liang, B. Kong, J. Zhang, J. Song, Q. Bao, G. P. Simon, S. P. Jiang and H. Wang, *Adv. Funct. Mater.*, 2015, **25**, 5768-5777.
 - 41 H. Zhang, S. Hwang, M. Wang, Z. Feng, S. Karakalos, L. Luo, Z. Qiao, X. Xie, C. Wang, D. Su, Y. Shao and G. Wu, *J. Am. Chem. Soc.*, 2017, **139**, 14143-14149.
 - 42 H. Chen, K. Shen, J. Chen, X. Chen and Y. Li, *J. Mater. Chem. A.*, 2017, **5**, 9937-9945.
 - 43 L. He, L. Li, T. Wang, H. Gao, G. Li, X. Wu, Z. Su and C. Wang, *Dalton Trans.*, 2014, **43**, 16981-16985.
 - 44 H. Zhang, J. Wei, J. Dong, G. Liu, L. Shi, P. An, G. Zhao, J. Kong, X. Wang, X. Meng, J. Zhang and J. Ye, *Angew. Chem. Int. Ed.*, 2016, **55**, 14310-14314.
 - 45 J. M. Lehn and R. Ziessel, *J. Organomet. Chem.*, 1990, **382**, 157-173.
 - 46 X. H. Lin, Y. L. Gao, M. Jiang, Y. F. Zhang, Y. D. Hou, W. X. Dai, S. B. Wang and Z. X. Ding, *Appl. Catal. B: Environ.*, 2018, **224**, 1009-1016.
 - 47 S. B. Wang, Y. D. Hou and X. C. Wang, *ACS Appl. Mater. Inter.*, 2015, **7**, 4327-4335. View Article Online
DOI: 10.1039/C8TA06151C
 - 48 J. Qin, L. Lin and X. Wang, *Chem. Commun.*, 2018, **54**, 2272-2275.
 - 49 W. Zhu, C. Zhang, Q. Li, L. Xiong, R. Chen, X. Wan, Z. Wang, W. Chen, Z. Deng and Y. Peng, *Appl. Catal. B: Environ.*, 2018, **238**, 339-345.
 - 50 J. Ran, M. Jaroniec and S.Z. Qiao, *Adv. Mater.*, 2014, **26**, 4607-4626.
 - 51 L. Liu, W. L. Fan, X. Zhao, H. G. Sun, P. Li, L. M. Sun, *Langmuir*, 2012, **28**, 10415-10424.



Activity and Selectivity Regulation through the Size of Cobalt Active
Sites in Photocatalytic CO₂ Reduction